Journal of Sound and Vibration (1999) **220**(5), 921–940
Article No. jsvi.1998.2006, available online at http://www.idealibrary.com.on IDEAL

PASSIVE ALLEVIATION OF MICRO-PRESSURE WAVES FROM TUNNEL PORTALS

T. AOKI

Graduate School of Engineering Sciences, *Kyushu University*, *Kasuga*, *Fukuoka* 816, *Japan*

AND

A. E. VARDY AND J. M. B. BROWN

Civil Engineering Department, *University of Dundee*, *Dundee DD*1 4*HN*, *Scotland*

(*Received* 7 *May* 1998, *and in final form* 12 *October* 1998)

When a high-speed train enters a tunnel, it generates a compression wave which propagates along the tunnel ahead of the train. A small proportion of the wave subsequently emerges from the exit portal of the tunnel as an impulsive wave. This so-called *micro-pressure wave* causes annoyance through low frequency noise and vibrations in the surrounding area. The objective of this paper is to determine the optimum dimensions of an expansion chamber at the tunnel exit portal for the purpose of reducing the micro-pressure wave. The effects of expansion chambers are investigated numerically and experimentally. Optimum proportions of a right-cylindrical chamber are found and a clear relationship is obtained between the total volume and the degree of attenuation of the micro-pressure wave.

1. INTRODUCTION

When trains pass through tunnels at high speed, pressure waves are generated and propagate back and forth along the tunnel. They are a potential source of discomfort to passengers on board the trains [1] and considerable effort has been devoted to reducing their effects. Methodologies for improving conditions for passengers include aerodynamic sealing of trains, connecting the tunnel to atmosphere by intermediate shafts and constructing long extension regions beyond portals [2].

Outside Japan, much less effort has been devoted to a second consequence of the pressure waves, namely the emission of small, higher frequency waves from tunnel exit portals during the internal reflection of the steepest parts of the main waves. Inside Japan, this topic has been studied for over 30 years and it is well understood [3]. There are three reasons for the geographical difference. First, the high-speed train era began in Japan. Second, many Japanese tunnels have been built using slab-track technology (no ballast). Third, many tunnels in Japan are close to areas of population. There are houses within 50 m of tunnel portals and

0022–460X/99/100921 + 20 $30.00/0

the micro-pressure waves cause doors and windows to rattle. The first two of these reasons are now equally applicable in several countries outside Japan.

Experience in Japan shows that the amplitude of the micro-pressure waves (and hence the degree of annoyance that they cause) correlates strongly with the *steepness* of the wavefront arriving at the exit portal and is almost independent of the *magnitude* of the wavefront. This result cannot be true universally, but it is nearly so in conventional tunnels because the *shapes* of the approaching wavefronts are always of a broadly similar form. If significantly different shapes existed, then account would need to be taken of their magnitudes as well as their associated rates of change of pressure.

Most research has been focused on reducing the steepness of the wavefront reaching the tunnel exit. Possibilities include building extension regions outside tunnel *entrance* portals (see, e.g., reference [4]) and/or elongating train noses. The objective of these methods of solution is to reduce the rate of change of pressure caused by the initiating event. Subsequent steepening as the wavefront propagates along the tunnel reduces the effectiveness, but sufficiently long hoods or noses can be highly effective.

Another possibility is to modify the wave propagation process by means of side branches along the tunnel itself. Maeda [5] showed this to be effective aerodynamically, but it might be more costly than portal extensions.

With sufficiently high train speeds, well-designed hoods at *exit* portals would be more effective than well-designed (but different) hoods at entrance portals. These speeds are not yet in operation, but they are being approached. Even at today's speeds, it may be valuable to use exit modifications in addition to entrance hoods [6, 7].

In the case of single-track tunnels with a predetermined direction of travel, portal modifications can be designed specifically for train entry and exit, respectively. In contrast, the portals of twin-track tunnels must act as entrances as well as exits and so the optimum design of any modification must take account of both purposes. Nevertheless, only *exit* requirements are considered herein.

1.1. REFLECTION AT TUNNEL EXIT

The disturbances emanating from tunnel exit portals are related to those emerging from gun muzzles [8], from rocket venturis [9] or exhaust systems of internal combustion engines [10]. From an analytical point of view, the phenomenon is inherently simpler because the gas (air) is nearly ideal and the pressure magnitudes are small. From a practical point of view, however, the large dimensions of tunnels (typically 8–10 m in diameter) restrict the range of visually acceptable solutions.

In parallel with research on passive devices such as those considered herein, there is other research on *active* methods of attenuation (see, e.g., references [11–15]). In all cases, it is important that modifications designed to improve external conditions should not significantly worsen conditions inside the tunnel [2, 16].

2. THEORETICAL BASIS

The numerical method is a TVD scheme, using a local characteristics approach with shock capturing. The method is summarized in this section; more detail has been given by Yee [17]. Herein, all pressure fluctuations are much smaller than those for which shocks deviate significantly from isentropic behaviour. Moreover, the wavefronts do not steepen sufficiently for true shocks to develop. The advantage of using this particular method of analysis is that it enables sudden changes in pressure (and velocity) to pass through the solution domain without significant numerical distortion.

Equations describing the adiabatic, inviscid, axi-symmetric flow of a perfect gas may be written in conservation form as

$$\partial \mathbf{U}/\partial t + \partial \mathbf{F}/\partial x + \partial \mathbf{G}/\partial y + \mathbf{W} = 0, \tag{1}$$

in which

$$\mathbf{U} = \begin{bmatrix} \rho \\ \rho u \\ \rho v \\ \rho e \end{bmatrix}, \quad \mathbf{F} = \begin{bmatrix} \rho u \\ \rho u^2 + p \\ \rho uv \\ (\rho e + p)u \end{bmatrix}, \quad \mathbf{G} = \begin{bmatrix} \rho v \\ \rho uv \\ \rho v^2 + p \\ (\rho e + p)v \end{bmatrix},$$

$$\mathbf{W} = \frac{1}{y} \begin{bmatrix} \rho v \\ \rho uv \\ \rho v^2 \\ (\rho e + p)v \end{bmatrix}, \tag{2}$$

where ρ is the mass density, u, v are the axial and radial velocity components, p is the pressure and e is the sum of the internal energy per unit mass and the kinetic energy per unit mass, namely

$$e = c_v T + \tfrac{1}{2}(u^2 + v^2), \tag{3}$$

where c_v is the specific heat capacity at constant density and T is the absolute temperature. (A list of symbols is given in the Appendix.)

The system is closed by the thermal equation of state for a perfect gas, namely

$$p = \rho R T, \tag{4}$$

where R is the gas constant. Herein the gas properties are taken for air to be $c_v = R/(\gamma - 1) = 718$ J/kg K and $R = 287$ J/kg K. The specific heat capacity at constant pressure is taken as $c_p = \gamma R/(\gamma - 1) = 1005$ J/kg K and so the ratio $\gamma = c_p/c_v$ is 1·400.

In the following development, the equations are used in a non-dimensional form, using ambient atmospheric conditions (p_{AT}, ρ_{AT} and c_{AT}) and the tube diameter D as reference parameters: namely,

$$p' \equiv \frac{p}{p_{AT}}, \qquad \rho' \equiv \frac{\rho}{\rho_{AT}}, \qquad u' \equiv \frac{u}{c_{AT}/\gamma^{1/2}},$$

$$v' \equiv \frac{v}{c_{AT}/\gamma^{1/2}}, \qquad t' \equiv \frac{t}{(D/c_{AT})\gamma^{1/2}}, \qquad x' \equiv \frac{x}{D}, \qquad y' \equiv \frac{y}{D}. \tag{5}$$

For clarity of presentation, the primes are omitted hereafter.

2.1. NUMERICAL SOLUTION

The equations are solved numerically by a second-order, symmetric, total variation diminishing (TVD) scheme [17] together with an operator splitting technique [18]. In this two-dimensional approach, each direction is treated in essentially the same manner as for one-dimensional flows. For brevity, only one direction is described.

The characteristic wavespeeds are the eigenvalues a^k of the Jacobian matrix $\partial\mathbf{F}/\partial\mathbf{U}$, namely

$$a^1 = u - c, \qquad a^2 = u, \qquad a^3 = u + c \tag{6}$$

where c is the local speed of sound relative to the flow. The right-eigenvector matrix is

$$\begin{bmatrix} 1 & 1 & 1 \\ u - c & u & u + c \\ H - uc & \frac{1}{2}u^2 & H + uc \end{bmatrix}, \tag{7}$$

where $H = c_p T + \frac{1}{2}(u^2 + v^2)$ is the stagnation enthalpy per unit mass. By using Roe's [19] approximate Riemann solver, the magnitudes of the jumps in the characteristic variables are expressed as

$$\alpha_{i+1/2} = \mathbf{R}^{-1}_{i+1/2}(U_{i+1} - U_i), \tag{8}$$

in which the subscript $(i + \frac{1}{2})$ denotes an average state between adjacent grid points i and $i + 1$ and $\mathbf{R}^{-1}$ is the inverse of the eigenvector matrix, namely

$$\mathbf{R}^{-1} = \begin{bmatrix} \frac{1}{2}(b_1 + u/c) & -\frac{1}{2}(ub_2 + 1/c) & \frac{1}{2}b_2 \\ 1 - b_1 & ub_2 & -b_2 \\ \frac{1}{2}(b_1 - u/c) & -\frac{1}{2}(ub_2 - 1/c) & \frac{1}{2}b_2 \end{bmatrix}, \tag{9}$$

where $b_1 = \frac{1}{2}(\gamma - 1)u^2/c^2$ and $b_2 = (\gamma - 1)/c^2$.

The solution at a particular position $i\Delta x$ and time $(n + 1)\Delta t$ is expressed in the form

$$U_{i,n+1} = U_{i,n} - \frac{\Delta t}{\Delta x}[\hat{\mathbf{F}}_{i+1/2,n} - \hat{\mathbf{F}}_{i-1/2,n}], \tag{10}$$

where $\hat{\mathbf{F}}$ denotes a *numerical* flux vector [17]. When solving by the local characteristic approach, $\hat{\mathbf{F}}$ is related to the true flux vector $\mathbf{F}$ by, typically,

$$\hat{\mathbf{F}}_{i+1/2} = \tfrac{1}{2}[\mathbf{F}_i + \mathbf{F}_{i+1} + \mathbf{R}_{i+1/2}\boldsymbol{\Phi}_{i+1/2}] \tag{11}$$

where $\mathbf{R}$ is the eigenvector matrix and $\boldsymbol{\Phi}$ is a vector designed to eliminate non-physical behaviour in regions of strongly varied flow, especially close to sudden changes in flow parameters. It includes (i) an "entropy correction function $\boldsymbol{\Psi}$" that ensures that the process converges only to physically possible solutions even though the conservation laws (equation (1)) include no constraints from the second law of thermodynamics, and (ii) a "limiter function $\mathbf{Q}$" that prevents numerical oscillations by restricting the magnitude of the numerical flux vector.

The elements of the vector $\boldsymbol{\Phi}$ have the form

$$\phi^k = -\frac{\Delta t}{\Delta x}(a^k)^2 Q^k - \psi(a^k)[\alpha^k - Q^k], \tag{12}$$

where the limiter function is given, typically, by

$$q^k_{i+1/2} = \text{minmod}\,[\alpha^k_{i-1/2}, \alpha^k_{i+1/2}, \alpha^k_{i+3/2}]. \tag{13}$$

The entropy correction function is

$$\psi(a^k) = \begin{Bmatrix} |a^k| & \text{when} \quad |a^k| \geqslant \delta \\ \dfrac{1}{2\delta}((a^k)^2 + \delta^2) & \text{when} \quad |a^k| < \delta \end{Bmatrix}, \tag{14}$$

in which δ is a small positive number, taken herein as 0·01.

2.2. BOUNDARY CONDITIONS AND INITIAL CONDITIONS

The solution space is the shaded region depicted in the upper part of Figure 1. A tube of diameter D has an expansion chamber of diameter d at its downstream end. There is an infinite baffle plate at the outlet. The length and height of the expansion chamber are denoted by ℓ and h ($=\frac{1}{2}[d - D]$) respectively and the width of the baffle plate is w.

The slip-wall condition is used at all solid surfaces and symmetric conditions are assumed at the centre-line. Null-reflection conditions are used at the outer edges of the region outside the tunnel portal, based on ambient atmospheric pressure.

Physical experiments. For comparisons with the experimental measurements reported herein, the initial condition is stationary flow at atmospheric pressure. The upstream boundary condition—at the left-hand end of Figure 1—is initially defined by the measured pressure history, smoothed to eliminate experimental noise. It converts automatically to a null-reflection condition when upstream-moving waves begin to arrive from the chamber.

Numerical experiments. For all simulations except those designed to reproduce the model experiments, the upstream boundary condition and the initial conditions are represented in the manner recommended by Ozawa [3]. He recognized that a large number of parameters can have a strong influence on the particular shape

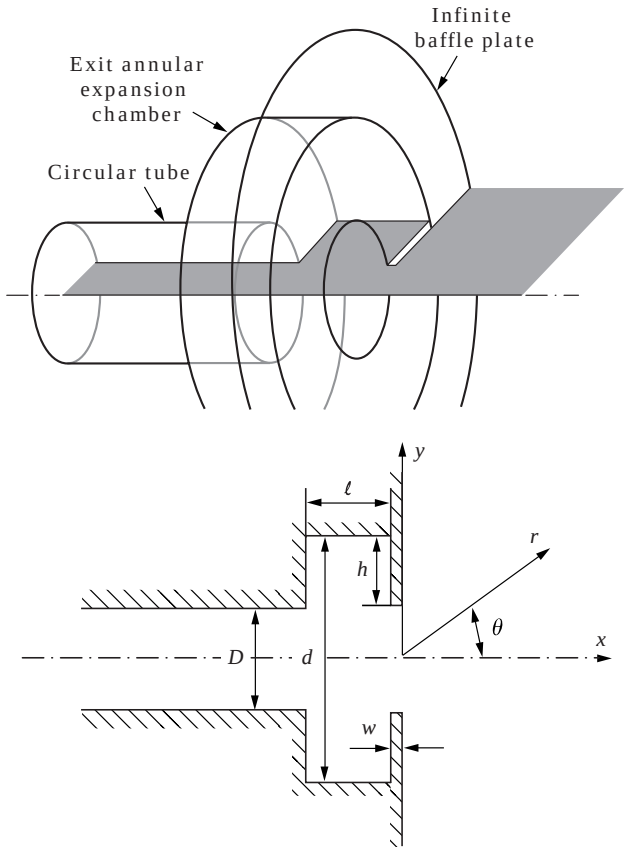

Figure 1. Expansion chamber geometry and computational field.

of the wavefront approaching the exit portal of a tunnel. Relevant parameters include the following: Tunnel: length, area, track type (ballast or slab), track eccentricity, portal shape; train: area, nose shape, underbody and pantograph geometry, speed.

Ozawa (who, at that time, worked for the Railway Technical Research Institute in Japan) had access to many pressure histories measured in tunnels. Following previous work by Yamamoto [20] he showed that steep wavefronts in slab-track tunnels resemble the typical shape illustrated in Figure 2, at least qualitatively. For the first few kilometres of propagation along a tunnel, inertial steepening dominates frictional resistance; thereafter, the reverse is true.

The pressure Δp at any position x along the curve in Figure 2 satisfies

$$\frac{\Delta p}{p_{AT}} = \frac{\Delta p^*}{p_{AT}}\left[\frac{1}{2} - \frac{1}{\pi}\tan^{-1}\left\{\frac{\pi x}{L}\right\}\right], \tag{15}$$

in which L is a length that is used to characterize the maximum steepness of the wavefront, Δp^* is the difference between the asymptotic pressures at $\pm\infty$ and p_{AT} denotes atmospheric pressure. Ozawa found that the pressure gradient $\Delta p^*/L$ has a crucial influence on the amplitude of the micro-pressure wave emitted from a

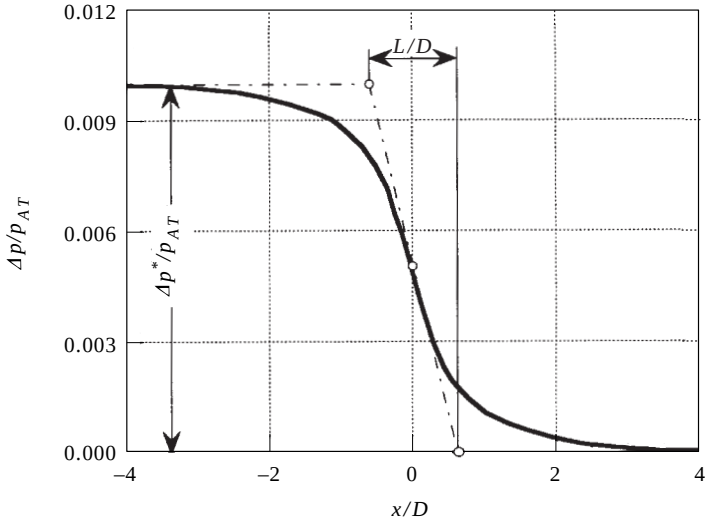

Figure 2. Idealized form of a train-entry wavefront.

simple tunnel portal. The relationship between these parameters is approximately linear.

Equation (15) applies throughout $-\infty < x < \infty$. To enable it to be used as an initial condition in the numerical analysis, its range is restricted to $-10\,D/3 < x < 10\,D/3$ and it is scaled to achieve $\Delta p = \Delta p^*$ at the upstream boundary ($x = -10\,D/3$) and $\Delta p = 0$ at the left-hand end of the expansion chamber ($x = 10\,D/3$). The scaling factor is approximately 1·03. The initial *velocity* distribution at $t = 0$ is deduced from (the scaled form of) equation (15) by assuming that no disturbance has propagated upstream. That is, the velocity at each point in the cross-section at any position x is set equal to $\Delta p/(\rho c)$ where ρ is the density of the air and c is the undisturbed speed of sound.

Null reflection conditions are assumed at the upstream boundary throughout $t > 0$. In practice, this ensures that the boundary pressure does not change until reflections begin to arrive from the expansion chamber.

3. COMPARISONS WITH EXPERIMENTAL MEASUREMENTS

The experimental apparatus used in the present work is a simple open-ended shock tube [16]. Its diameter is 76 mm and its overall length is 6·1 m. The high pressure section, which has a length of 2·7 m, is initially separated from the low pressure region by a paper diaphragm. When the upstream pressure is gradually increased, the diaphragm ruptures passively. Hitherto, all work with this facility had been carried out by using dry diaphragms, leading to abrupt rupture and very steep wavefronts. Following an inspired suggestion by Setoguchi [21], however, the present results include cases with slightly wet paper, leading to less abrupt rupture. Typically the bursting pressures of the dry and wet diaphragms are about 12 and 6 kPa, respectively.

The geometry of the expansion chamber used in the present study is illustrated in Figure 1. All chambers were axi-symmetric and, in most tests, there was a baffle plate at the downstream end. In the following theoretical analysis, this is treated as being infinite. In the apparatus, it was a wooden sheet of sufficiently large dimensions for its finite size to be irrelevant herein. There is evidence, however, that the structural support for the plate was not sufficiently stiff. This is a probable explanation for a discrepancy between measured and predicted pressures on the plate (see section 3.2). Agreement elsewhere is encouraging.

Piezo-electric quartz pressure transducers (Kistler type 7031) were flush-mounted on the apparatus (i) 253 mm upstream of the chamber and (ii) on the baffle plate at $y = 152$ mm (i.e., $y/D = 2$). Two other transducers were supported externally (iii) at $r = 114$ mm (i.e., $r/D = 1{\cdot}5$), $\theta = 0^\circ$ and (iv) at $r = 114$ mm, $\theta = 45^\circ$.

3.1. SIMPLE OPEN END

Typical experimental pressure-time records are shown in Figures 3 and 4 for abrupt and gradual diaphragm rupture, respectively. In these cases, there is no expansion chamber, but there is a baffle plate (see Figure 1).

The upper pressure traces in each figure show measured pressure histories at the upstream pressure transducer together with the corresponding smoothed versions that have been used to define the upstream boundary condition in the numerical calculations. In Figure 3, the smoothed curve is an abrupt pressure increase followed by constant pressure until reflections begin to arrive from the portal. In Figure 4, the leading part of the wavefront resembles the $\tan^{-1}$ shape illustrated in Figure 2.

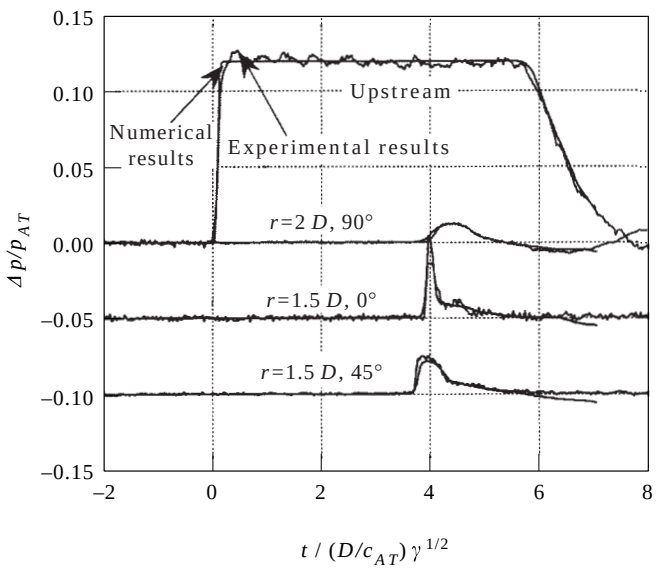

Figure 3. Measured and predicted pressure histories: simple portal (incident shock wave ($L/D = 0$), $\Delta p^* = 12{\cdot}1$ kPa).

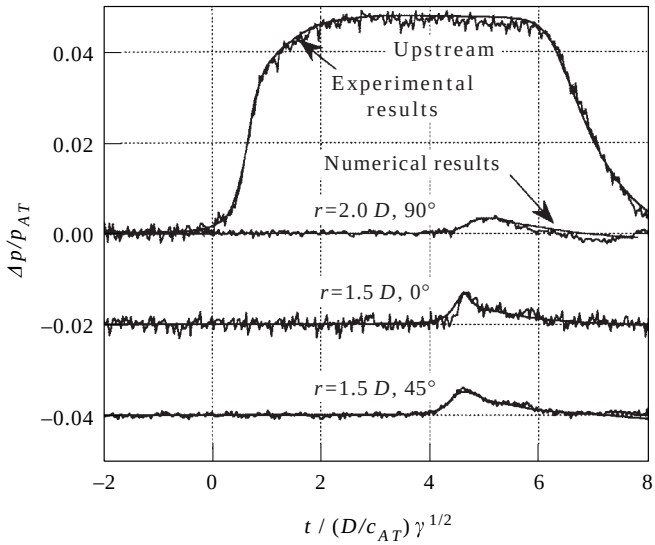

Figure 4. Measured and predicted pressure histories: simple portal (incident wave front $L/D = 1{\cdot}02$, $\Delta p^* = 4{\cdot}85$ kPa).

The lower three traces in each figure show the corresponding pressures at pressure transducers outside the portal, these traces being offset for clarity. The positions of the transducers are defined by the co-ordinates r and θ defined in Figure 1. The smooth curves at these locations are theoretical predictions obtained as described in section 2, by using a numerical grid size of $\Delta x = \Delta y = D/28$.

The shapes of the pressure histories outside the tunnel are characteristic of the micro-pressure wave phenomenon. When an incident step wavefront reflects/transmits at a simple portal, the resulting pressure field outside the tunnel may be approximated by a single pulse propagating radially, but not uniformly in all directions. The greatest magnitude occurs on the centre-line ($\theta = 0^\circ$) and successively smaller magnitudes—but longer durations—are experienced with increasing θ. These trends are especially obvious with the abrupt incident pressure change (Figure 3), but they can also be seen with the more gentle wavefront (Figure 4).

With one exception, agreement between the experimental and theoretical curves is sufficient to promote confidence in the numerical tool. The exception is on the centre line ($r/D = 1{\cdot}5$, $\theta = 0^\circ$) in Figure 3 where the numerical peak exceeds the measured value. The cause of this discrepancy can be traced to the assumption that the initial pressure change at the upstream boundary occurs in exactly one time step which, in this instance, is smaller than the true rise time—as can be seen in the figure. Much closer agreement can be obtained by tuning the time step to the particular application, but this would obstruct the underlying purposes of the comparisons. It is considered more useful to highlight the difficulty than to select an ideal time step in order to hide it. One advantage is that this enables comparisons at the other positions in the figure to be regarded as a demonstration of lower sensitivity to grid-size. The 45° position is the one that is most important for practical purposes.

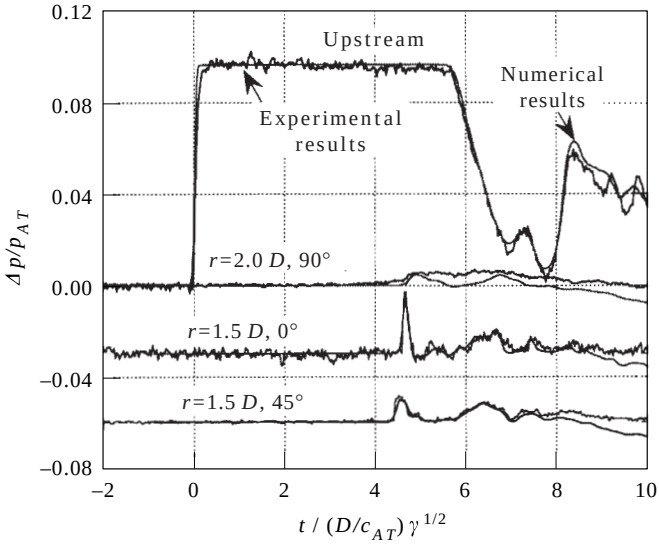

Figure 5. Measured and predicted pressure histories: with expansion chamber (incident shock wave ($L/D = 0$), $\Delta p^* = 9{\cdot}77$ kPa, $h/D = 1{\cdot}06$, $\ell/D = 0{\cdot}64$, $w/D = 0{\cdot}24$).

The *physical* outcome is also extremely sensitive to rates of change as large as that considered in Figure 3. In practice, however, such large rates of change do not occur in railway tunnels; the conditions shown in Figure 4 are much more typical.

3.2. EXPANSION CHAMBER

Figures 5 and 6 show the corresponding pressure histories when there is an expansion chamber ($d/D = 3{\cdot}12$, $h/D = 1{\cdot}06$, $\ell/D = 0{\cdot}64$, $w/D = 0{\cdot}24$) just

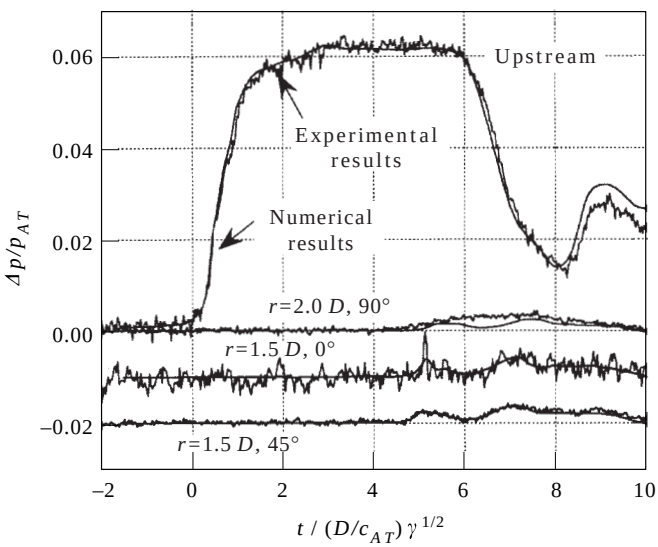

Figure 6. Measured and predicted pressure histories: with expansion chamber (incident wave front $L/D = 1{\cdot}40$, $\Delta p^* = 6{\cdot}22$ kPa, $h/D = 1{\cdot}06$, $\ell/D = 0{\cdot}64$, $w/D = 0{\cdot}24$).

upstream of the exit portal. There is a striking difference between these results and those found with a simple portal (Figures 3 and 4). Instead of a single, pronounced peak, the pressure histories exhibit two, more gentle peaks. Indeed, in the case of the more gradual incident wavefront (Figure 6), the amplitude of the second pulse exceeds that of the first.

The agreement between the measured and predicted curves is quite good except: (i) on the baffle plate ($r/D = 2$, $\theta = 90^\circ$) for both examples and (ii) on the centre-line ($r/D = 1{\cdot}5$, $\theta = 0^\circ$) at $t \approx 1{\cdot}35$ ms in Figure 6. The first of these locations is on the baffle plate that was subsequently found to have been inadequately supported (see section 3, second paragraph). There was no equivalent problem with the simple portal (see section 3.1) because that plate was mounted directly on the tube and was suitably braced.

The second discrepancy is at the leading edge of the micro-pressure wave, where the measured value exhibits a short-lived peak that it not predicted numerically. The cause of this discrepancy has not been tracked down, but the effect is believed to be physical because it is also found in other tests results (not shown). One possibility is that numerical dispersion is too great to permit the transmission of such short-lived events with achievably small grid sizes. Another possibility is that viscous effects have non-negligible influence on the wave transmission/reflection processes at the ends of the chamber. Whatever the reason, the most important deduction from all of Figures 3–6 is that the numerical predictions at the crucial 45° location are of sufficient accuracy for realistic deductions to be made about the influence of expansion chambers.

The existence of two (or more) pulses is a characteristic consequence of the chamber. The relative magnitudes of the peaks depend upon the chamber geometry. As shown in these and subsequent figures, some geometries cause the first pulse to be greatest; others cause the second to be greater. An implicit objective of the following development is to select the shapes of expansion chambers to equalize the two pulses, thereby minimizing the maximum amplitude.

The origins of the pulses can be deduced from Figure 7 which shows computed pressure contours at successive instants. In Figure 7(a), the incident wavefront has just reached the beginning of the expansion chamber. In Figure 7(b), there is a negative reflection (R1) and a reduced positive transmission to the end of the chamber. In Figure 7(c), the first pulse (P1) is leaving the tunnel and a positive reflection is beginning to develop on the end wall of the chamber. This gives rise to both P2 and R2 in Figure 7(d). The subsequent reflection of R2 at the upstream end of the chamber gives rise to a second pair of pulses (only P3 is labelled in Figure 7(e), but P4 can also be seen). Further reflections give rise to additional pulses, but their magnitudes are relatively small.

4. OPTIMIZATION

Figure 8 shows predicted micro-pressure waves for two chambers, one labelled $h/D = 0{\cdot}222$ and the other labelled $h/D = 0{\cdot}444$. The lengths of the chambers are equal ($\ell/D = 1{\cdot}0$) so one is more than twice the volume of the other (herein the "volume" of a chamber is deemed to be the *extra* volume in comparison with the

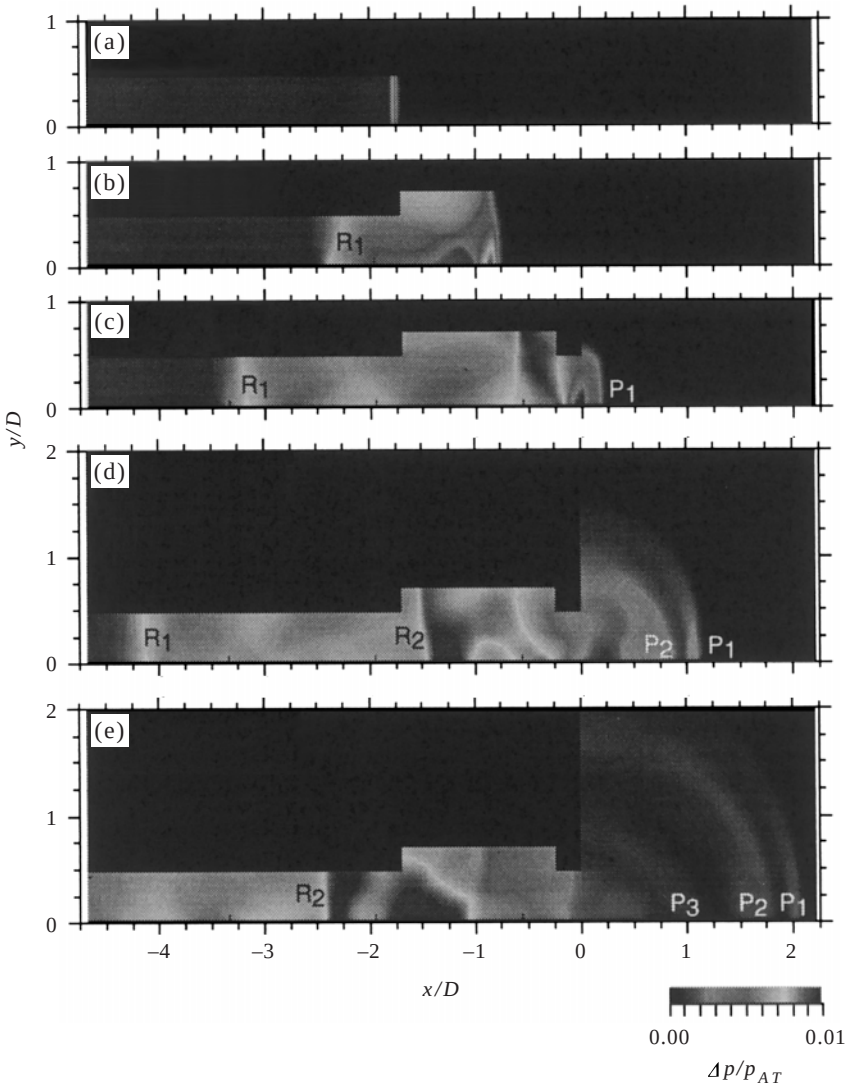

Figure 7. Predicted pressure contours; with expansion chamber (incident shock wave ($L/D = 0$), $\Delta p^* = 1$ kPa, $h/D = 0{\cdot}24$, $\ell/D = 1{\cdot}5$, $w/D = 0{\cdot}24$). (a) $t' = 0$; (b) $t' = 0{\cdot}81$; (c) $t' = 1{\cdot}63$; (d) $t' = 2{\cdot}44$; (e) $t' = 3{\cdot}26$.

simple tunnel). The predictions are shown at the position ($r/D = 2$, $\theta = 45^\circ$) which is a standard comparison position in Japan (see, e.g., reference [3]).

The influences of the chambers are shown for two incident wavefronts, namely $L/D = 0$ and $L/D = 1$ (see Figure 2) and, by inspection, strong differences exist in the detailed shapes of the micro-pressure waves. The continuous line ($h/D = 0{\cdot}444$, $L/D = 0$) has three peaks, of which the second is the greatest. In contrast, the curve labelled $h/D = 0{\cdot}222$, $L/D = 0$ has only two well defined peaks and the curve labelled $h/D = 0{\cdot}222$, $LD = 1$ has only one.

Herein, the effectiveness of each particular chamber with any particular incident wavefront is deemed to be characterized by Δp_{max}, the amplitude of the greatest

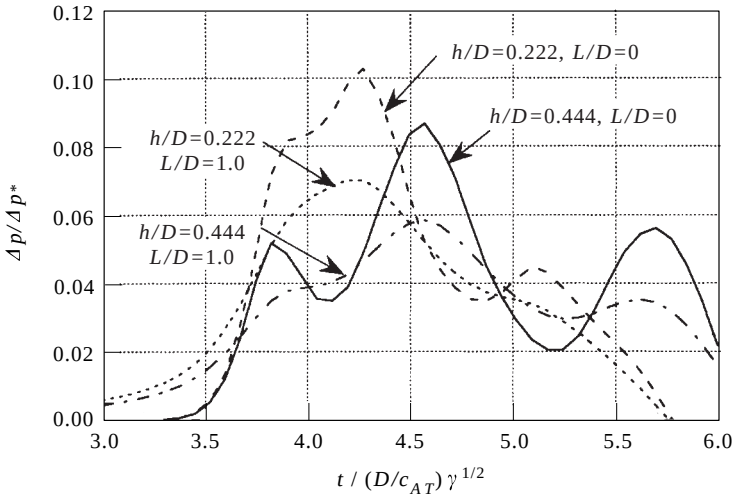

Figure 8. Predicted micro-pressure wave histories: influence of expansion chamber ($\Delta p^*/p_{AT} = 0{\cdot}079$, $\ell/D = 1$, $w/D = 0{\cdot}0555$, $r/D = 2$, $\theta = 45°$).

peak, irrespective of how many peaks exist. For simple portals, this is the parameter that is primarily responsible for perceived nuisance outside the tunnel. It is not certain that the same will be true when an expansion chamber exists, but no more reasonable method of comparison has been identified.

No further pressure histories are shown herein. Many simulations are needed for the development of the following figures and it is neither practical nor necessary to display the raw data. Instead, each result is simply characterized by the amplitude of the largest pulse, designated Δp_{max}.

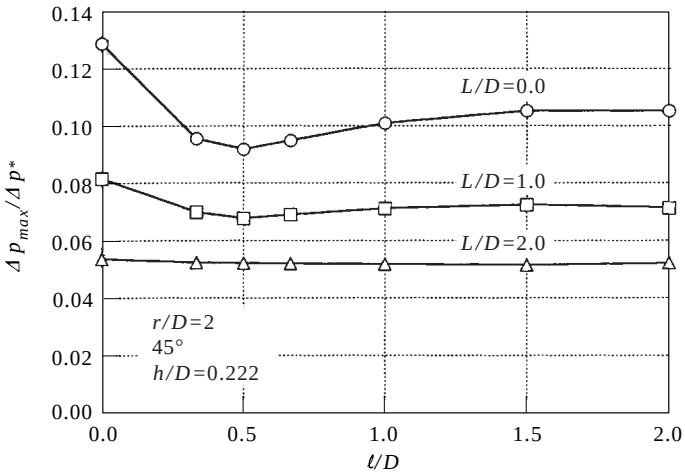

Figure 9. Influence of chamber length on micro-pressure wave amplitude (the chamber height $h = 0{\cdot}222\ D$ is relatively small, $\Delta p^*/p_{AT} = 0{\cdot}079$, $w/D = 0{\cdot}0555$).

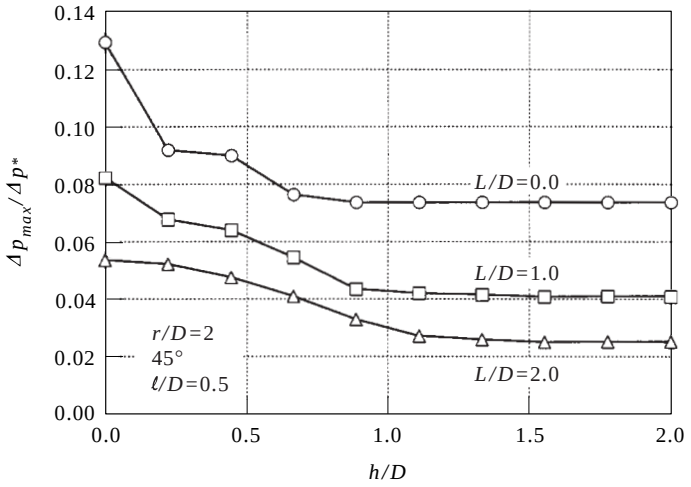

Figure 10. Influence of chamber height on micro-pressure wave amplitude (the chamber length $\ell = 0{\cdot}5\ D$ is relatively small, $\Delta p^*/p_{AT} = 0{\cdot}079$, $w/D = 0{\cdot}0555$).

4.1. LENGTH OF CHAMBER

Figure 9 illustrates the influence of the length of the chamber (ℓ/D) when its height is maintained constant ($h/D = 0{\cdot}222$). The results presented for $\ell/D = 0$ denote the case with no chamber so the figure enables a rapid visual assessment of the effectiveness of different lengths of chamber. It is apparent, for instance, that the influence on short wavefronts (small L/D) is greater than that on longer wavefronts. Also, increases in the chamber length do not necessarily lead to improved performance even though they imply greater volumes of excavation.

Consider first the results for a sudden wavefront ($L/D = 0$). With no chamber (i.e., $\ell/D = 0$) the maximum micro-pressure amplitude is $\Delta p_{max}/\Delta p^* \approx 0{\cdot}0103$, where Δp^* is the strength of the incident wave. With successively longer chambers, the amplitude of the first peak in the micro-pressure wave history reduces, but the amplitude of the second peak increases. When ℓ/D is smaller than about 0·5, the first peak dominates, but thereafter, the second peak is more important. Thus, there is an optimum length which for this particular chamber height, is about $\ell/D = 0{\cdot}5$.

A similar result is obtained with the more gentle incident wavefront, $L/D = 1$, but the benefit of the chamber is less great than for $L/D = 0$. Even less benefit is obtained for $L/D = 2$. This implies that the optimum dimensions of a chamber might be quite strongly dependent upon the steepness of the incident wavefronts: i.e. different chamber shapes (and sizes) might be preferred in different tunnels.

The particular results in Figure 9 apply only for a chamber with a stipulated height of $h = 0{\cdot}222D$. It is shown in the following paragraphs that larger heights offer greater benefit, especially with longer wavefronts. Typically, the optimum chamber height exceeds the optimum length—greatly so in the case of large L/D.

4.2. HEIGHT OF CHAMBER

Figure 10 illustrates the influence of the height of the chamber for the particular case of $\ell/D = 0{\cdot}5$. The results differ qualitatively from those obtained in Figure 9. In particular, no optimum height is found. Instead, successive increases in height yield increasing benefit until the curves become asymptotic to limiting values when h/D exceeds about 1·0. The existence of an asymptote arises because of the time required for waves to pass up and down the chamber. The time of arrival of reflections from the top of the chamber eventually becomes too great for any effect to be experienced on the main pulses of the micro-pressure waves.

The time interval between the first two pulses depends primarily on ℓ/D, the length of the chamber, but also on L/D, the length of the wavefront. It follows that the limiting height should increase with increasing values of these parameters. Figure 10 demonstrates the dependence on the wavelength; other results (not shown explicitly) demonstrate the dependence on the chamber length.

4.3. SHAPE OF CHAMBER

Figures 9 and 10 are specific cases for particular values of the chamber height h/D and length ℓ/D, respectively. Attention now moves to the optimum combination of these parameters, that is to the best *shape* of chamber. Ideally, this would be found to be independent of (i) the chamber *size* and (ii) the length of the incident wavefront. In practice, however, this is not quite so.

Figure 11 shows two sets of three curves, each set being valid for a particular chamber volume. The various points on any particular curve correspond to different combinations of height and length, chosen to yield the same volume $V = \pi(D + h)h\ell$. For example, the uppermost curves in the figures are applicable for a chamber volume of $\frac{1}{2}V_0$ where $V_0 = \frac{1}{4}\pi D^3$ is a reference magnitude, namely the volume of a region of tunnel of length D. For the particular case of $L/D = 2$, for example, the optimum height of chamber is $h/D \approx 0{\cdot}475$ and it follows that the optimum length is $\ell/D \approx 0{\cdot}178$. The optimum shape for this particular case is therefore $h/\ell \approx 2{\cdot}67$.

The lower set of curves in Figure 11 is applicable for a much larger chamber with a volume of $2V_0$. For this case, the optimum height for a wavefront of length $L/D = 2$ is approximately $h/D \approx 0{\cdot}83$ and the corresponding length is $\ell/D \approx 0{\cdot}33$. The optimum shape is therefore $h/\ell \approx 2{\cdot}5$.

The uppermost curve in Figure 12 has been obtained by repeating this process for additional chamber volumes. For the relatively long wavefront considered above ($L/D = 2$), the optimum chamber shape is not strongly dependent on the overall size. A similar result is obtained for a step wavefront (curve labelled $L/D = 0$ in Figure 12), but the optimum shape is different ($h/\ell \approx 1{\cdot}5$). This is unfortunate for designers because it implies a need to know which wavefront is most important for the particular tunnel under design. In practice, however, the nature of the incident wavefront is influenced by many factors that may change during the lifetime of a tunnel—e.g., train nose shape, train speed, tunnel entrance shape.

The intermediate curve in Figure 12 (i.e., $L/D = 1{\cdot}0$) shows a different behaviour from the other two, the optimum chamber shape being strongly

dependent on the chamber size. For the smallest volume considered ($0{\cdot}5V_0$), the dimensions $h/D \approx 0{\cdot}36$ and $\ell/D \approx 0{\cdot}25$ are similar to those preferred for an abrupt wavefront. For the largest ($2V_0$), they are the same as those preferred for longer wavefronts, namely $h/D \approx 0{\cdot}83$ and $\ell/D \approx 0{\cdot}50$.

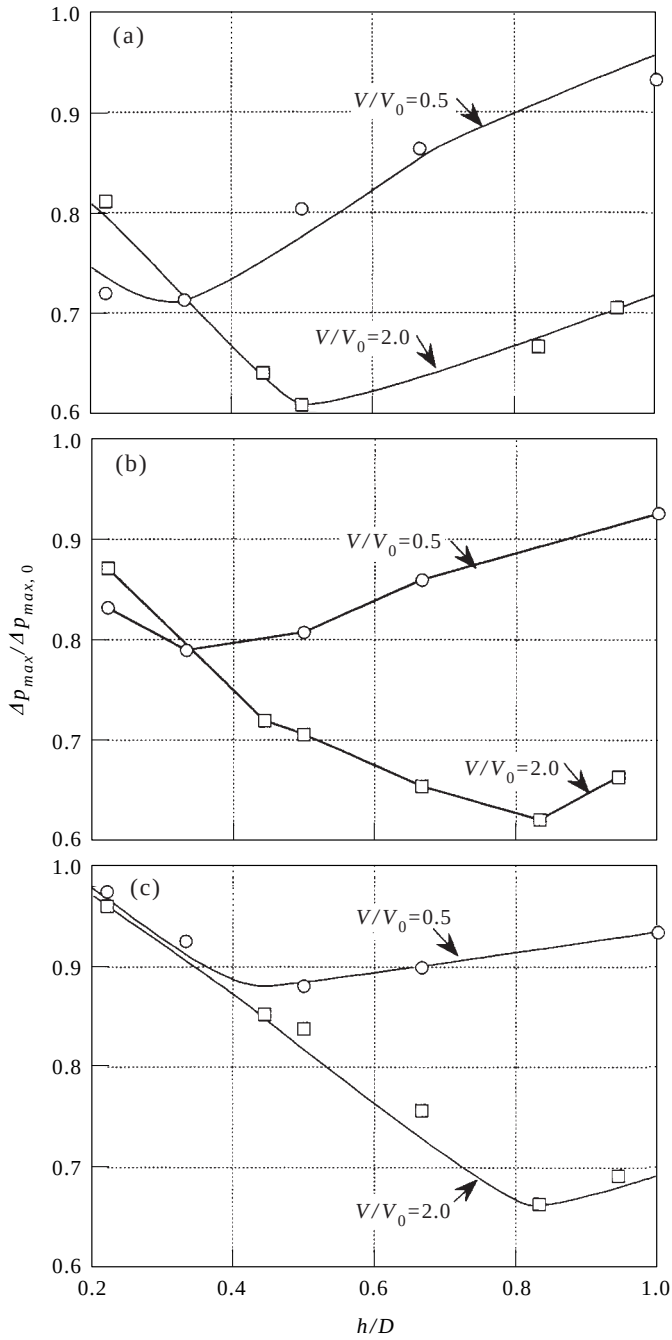

Figure 11. Influence of chamber height on micro-pressure wave amplitude (the chamber length ℓ is adjusted to achieve a constant chamber volume). (a) $L/D = 0$; (b) $L/D = 1$; (c) $L/D = 2$.

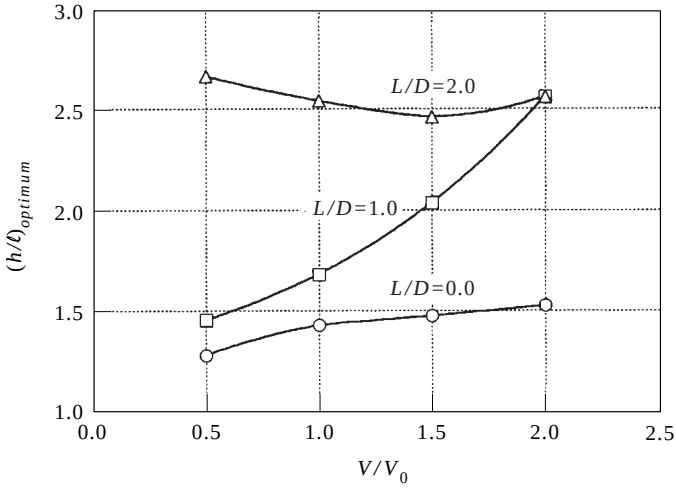

Figure 12. Influence of chamber size V/V_0 and wavefront steepness L/D on the optimum shape of a chamber.

In a practical design, the best chamber shape for any particular volume (and hence cost) will depend upon the expected range of wavelengths. A suitable strategy would be to choose the shape that provides greatest benefit for the steepest incident wavefront that is expected to occur. This will ensure that the greatest benefit is obtained when it is most needed. The chosen shape would be non-optimum for longer wavelengths, but these are less important than the steeper ones. Moreover, the proportional reduction in benefit will usually be small (see Figure 11).

4.4. MAXIMUM REDUCTION IN PRESSURE

Figure 13 shows the maximum micro-pressure wave amplitudes resulting from chambers of optimum shape. Consider, for example, a chamber of size $V = 2V_0$.

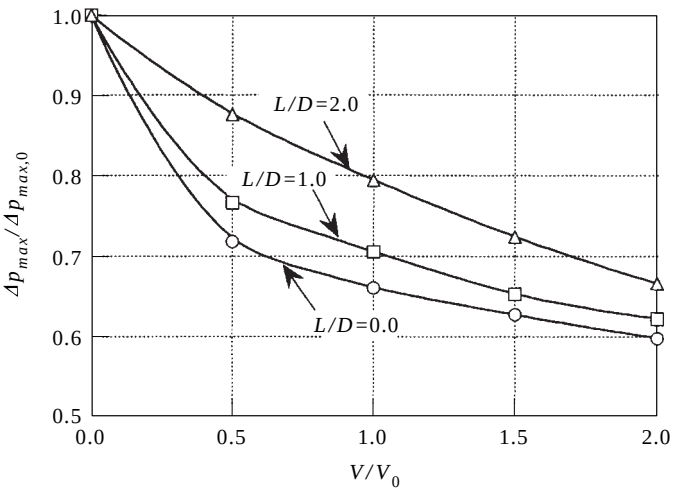

Figure 13. Amplitudes of micro-pressure waves; optimum chamber shapes.

With an incident wavefront satisfying $L/D = 1{\cdot}0$, the maximum rise is approximately 64% of the value with no chamber. That is, the peak has reduced by 36% from the case with no chamber. This is achieved with a chamber of shape $h/\ell \approx 2{\cdot}5$ (see Figure 12), which implies that $h/D \approx 0{\cdot}83$ and $\ell/D \approx 0{\cdot}33$.

In some cases, reductions of these amounts might provide sufficient reduction in the magnitudes of micro-pressure waves. More often, however, greater percentage reductions are likely to be needed and so either (a) chambers with volumes in excess of $2V_0$ will be needed or (b) other methods of alleviation must be considered.

Expansion chambers such as those considered herein are simple and can be expected to perform reliably. They may be a valuable *additional* counter-measure even when they do not provide sufficient relief by themselves.

5. CONCLUSIONS

Simple expansion chambers close to a tunnel exit portal can cause significant reductions in the amplitudes of micro-pressure waves propagating outside the tunnel.

The optimum shape of such chambers depends upon the steepness of the reflecting wavefront. Greatest percentage reductions are achieved for the steepest wavefronts.

When a range of steepnesses of incident wavefronts is expected, the chamber shape should be optimized for the steepest case that is considered feasible. This will provide greatest benefit when it is most needed. In most cases, this shape will also perform well with less steep wavefronts even though it is not optimum.

For any particular incident wavefront steepness, the optimum shape of the chamber is dependent on the chamber size (Figure 12). For the steep wavefronts of greatest relevance herein, however, the dependence is not strong.

Typically, a well-designed chamber with a volume of only V_0 (i.e., $\frac{1}{4}\pi D^3$) may cause a reduction of about 30% in the magnitudes of micro-pressure waves. This is in addition to reductions resulting from other modifications (e.g., at the tunnel entry).

ACKNOWLEDGMENT

The authors would like to express their appreciation for technical guidance from Professor K. Matsuo of Kyushu University and Professor H. Kashimura of Kitakyushu College of Technology. Financial assistance from The British Council is gratefully acknowledged.

REFERENCES

1. R. G. Gawthorpe 1991 *7th International Symposium on the Aerodynamics and Ventilation of Vehicle Tunnels*, *Brighton*, 173–188. Pressure comfort criteria for rail tunnel operations.

2. A. E. Vardy 1978 *Journal of Sound and Vibration* **59**, 577–589. Reflection of step-wavefronts from perforated and flared tube extensions.
3. S. Ozawa 1979 *Railway Technical Research Report of Japanese National Railways* **1121**, 1–92. Study of micro-pressure wave radiated from a tunnel exit (in Japanese).
4. S. Ozawa, T. Maeda, T. Matsumura, K. Uchida, H. Kajiyama and K. Tanemoto 1991 7*th International Symposium on the Aerodynamics and Ventilation of Vehicle Tunnels*, *Brighton*, 253–266. Countermeasures to reduce micropressure waves radiating from exits of Shinkansen tunnels.
5. T. Maeda 1982 *Quarterly Report of the Railway Technical Research Institute Japan* **23**, 34–37. Reduction of micro pressure waves radiated from tunnel exit portal by branches in tunnel.
6. M. Zeutzius, S. Matsuo, T. Nakano, T. Setoguchi and K. Kaneko 1996 9*th International Symposium on Transport Phenomena in Thermal-Fluids Engineering*, 303–308. Passive control of impulsive noise caused by unsteady compression wave.
7. K. Ehrendorfer and H. Sockel 1997 9*th International Symposium on the Aerodynamics and Ventilation of Vehicle Tunnels*, *Aosta*, 863–876. The influence of measures near the portal of railway tunnels on the sonic boom.
8. P. S. Westine 1969 *Shock and Vibration Digest Bulletin* **39**, 139–149. The blast fluid about the muzzle of guns.
9. J. L. Stollery, K. C. Pham and K. P. Garry 1981 13*th International Symposium on Shock Tubes and Waves*, 781–789. Simulation of blast fields by hydraulic analogy.
10. N. Sekine, S. Matsumura, K. Takayama, O. Onodera and K. Itoh 1988 *Transactions of the Japan Society of Mechanical Engineering* **54**, 527–531. Initiation and propagation of shock wave in the exhaust pipe of an internal combustion engine (in Japanese).
11. T. Aoki, Y. Harita, Y. Noguchi, Y. Nakagawa, N. Kondoh and K. Matsuo 1991 *International Symposium on Active control of Sound and Vibration*, 291–296. Investigations of active control of impulsive noise.
12. T. Maeda, T. Matsumura and K. Uchida 1992 *Railway Technical Research Institute Report* **16**(3), 39–46. Reduction of micro-pressure wave radiating from tunnel exit by dense spraying of water droplets in tunnel (in Japanese).
13. M. Nishimura, M. Kondo, K. Iwamoto and Y. Tsujimoto 1994 *Internoise* '94, 1383–1388. Active attenuation of impulsive noise from a railway tunnel exit.
14. M. Liang, T. Kitamura, T. Maeda, S. Yamada, T. Kosaka, K. Miyata and S. Yamada 1995 *Journal of the Acoustical Society of Japan* (*E*) **16**(6), 363–368. Active attenuation of tunnel pressure wave with negative pressure gradient generated by positive pressure.
15. T. Setoguchi, K. Matsuo, T. Aoki, N. Kita, K. Iwamoto, Y. Tsujimoto and K, Kaneko 1995 *Transactions of the Japan Society of Mechanical Engineers* **61–587**, 129–134. A study of negative impulse wave generator for reducing impulsive noise (in Japanese).
16. J. M. B. Brown and A. E. Vardy 1994 *Journal of Sound and Vibration* **73**, 95–111. Reflections of pressure waves at tunnel portals.
17. H. C. Yee 1987 *NACA TM*-89464, 1–127. Upwind and symmetric shock-capturing schemes.
18. G. A. Sod 1977 *Journal of Fluid Mechanics* **83**, 785–794. Numerical study of a converging cylindrical shock.
19. P. L. Roe 1981 *Journal of Computational Physics* **43**, 357–372. Approximate Riemann solvers, parameter vectors, and difference schemes.
20. A. Yamamoto 1977 *Physical Society of Japan* **1977**, 4P-H-4. Micro-pressure wave radiated from tunnel exit (in Japanese).
21. T. Setoguchi 1996 Private communication.

APPENDIX: LIST OF SYMBOLS

a characteristic speed (equation (6))
b matrix elements (equation (9))
c speed of sound
c_p specific heat capacity at constant pressure
c_v specific heat capacity at constant density
D diameter of tube/tunnel
d diameter of chamber
e specific internal energy
$\mathbf{F}$ flux vector
$\hat{\mathbf{F}}$ numerical flux vector
$\mathbf{G}$ vector defined in equations (2)
H specific stagnation enthalpy
h height of chamber (see Figure 1)
L length of wavefront (see Figure 2)
ℓ length of chamber (see Figure 1)
p pressure
Δp gauge pressure ($\equiv p - p_{AT}$)
Δp^* amplitude of $\tan^{-1}$ wavefront (equation (15))
Q element of limiter function vector $\mathbf{Q}$
R gas constant
$\mathbf{R}$ eigenvector matrix (equation (7))
r spherical co-ordinate (see Figure 1)
T temperature
t time
$\mathbf{U}$ vector defined in equation (2)
u axial component of velocity
V volume of chamber (excess over simple tunnel volume)
V_0 reference volume ($\frac{1}{4}\pi D^3$)
v radial component of velocity
$\mathbf{W}$ vector defined in equations (2)
w width of baffle plate (see Figure 1)
x axial co-ordinate
y axi-symmetric radial co-ordinate (see Figure 1)

Greek characters

α jumps in characteristic variables
φ ratio of principal specific heat capacities
δ small positive number (equation (13))
θ spherical co-ordinate (Figure 1)
ρ mass density
$\mathbf{\Phi}$ numerical viscosity vector
ϕ element of vector $\mathbf{\Phi}$
ψ element of entropy correction vector $\mathbf{\Psi}$

Superscripts

k matrix row number
$'$ non-dimensional parameter

Subscripts

AT atmospheric condition
i spatial grid number
n temporal grid number
0 reference condition